

## **Pore-Scale Visualization of Hydrogen Storage in a Sandstone at Subsurface Pressure and Temperature Conditions: Trapping, Dissolution and Wettability**

Jangda, Zaid; Menke, Hannah; Busch, Andreas; Geiger, Sebastian; Bultreys, Tom; Lewis, Helen; Singh, Kamaljit

**DOI**

[10.1016/j.jcis.2022.09.082](https://doi.org/10.1016/j.jcis.2022.09.082)

**Publication date**

2022

**Document Version**

Final published version

**Published in**

Journal of Colloid and Interface Science

**Citation (APA)**

Jangda, Z., Menke, H., Busch, A., Geiger, S., Bultreys, T., Lewis, H., & Singh, K. (2022). Pore-Scale Visualization of Hydrogen Storage in a Sandstone at Subsurface Pressure and Temperature Conditions: Trapping, Dissolution and Wettability. *Journal of Colloid and Interface Science*, 629 (2023), 316-325. <https://doi.org/10.1016/j.jcis.2022.09.082>

**Important note**

To cite this publication, please use the final published version (if applicable). Please check the document version above.

**Copyright**

Other than for strictly personal use, it is not permitted to download, forward or distribute the text or part of it, without the consent of the author(s) and/or copyright holder(s), unless the work is under an open content license such as Creative Commons.

**Takedown policy**

Please contact us and provide details if you believe this document breaches copyrights. We will remove access to the work immediately and investigate your claim.



# Pore-scale visualization of hydrogen storage in a sandstone at subsurface pressure and temperature conditions: Trapping, dissolution and wettability

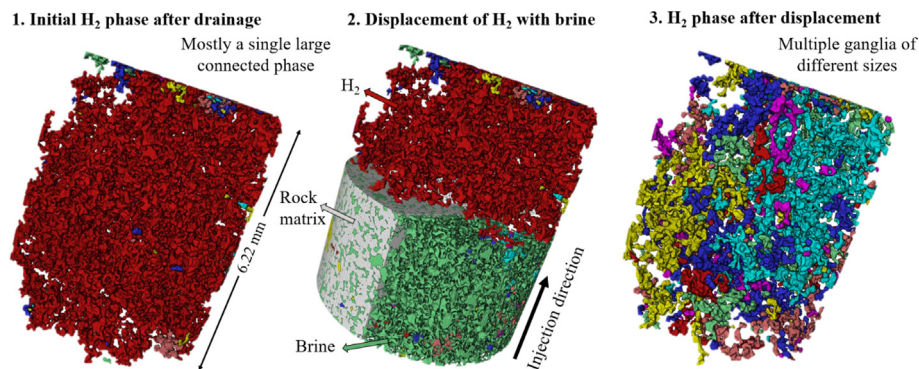
Zaid Jangda<sup>a,\*</sup>, Hannah Menke<sup>a</sup>, Andreas Busch<sup>a</sup>, Sebastian Geiger<sup>b</sup>, Tom Bultreys<sup>c</sup>, Helen Lewis<sup>a</sup>, Kamaljit Singh<sup>a</sup>

<sup>a</sup> Institute of GeoEnergy Engineering, Heriot-Watt University, EH14 4AS Edinburgh, United Kingdom

<sup>b</sup> Department of Geoscience and Engineering, Delft University of Technology, 2628 CN Delft, Netherlands

<sup>c</sup> UGCT/PProGress, Department of Geology, Ghent University, 9000 Ghent, Belgium

## GRAPHICAL ABSTRACT



## ARTICLE INFO

### Article history:

Received 10 July 2022

Revised 12 September 2022

Accepted 15 September 2022

Available online 20 September 2022

### Keywords:

Underground hydrogen storage

*In situ* flow experiment

3D X-ray visualization

Hydrogen wettability

## ABSTRACT

**Hypothesis:** Underground hydrogen (H<sub>2</sub>) storage is a potentially viable solution for large-scale cyclic H<sub>2</sub> storage; however, the behavior of H<sub>2</sub> at subsurface pressure and temperature conditions is poorly known. This work investigates if the pore-scale displacement processes in H<sub>2</sub>-brine systems in a porous sandstone can be sufficiently well defined to enable effective and economic storage operations. In particular, this study investigates trapping, dissolution, and wettability of H<sub>2</sub>-brine systems at the pore-scale, at conditions that are realistic for subsurface H<sub>2</sub> storage.

**Experiments:** We have performed *in situ* X-ray imaging during a flow experiment to investigate pore-scale processes during H<sub>2</sub> injection and displacement in a brine saturated Bentheimer sandstone sample at temperature and pressure conditions representative of underground reservoirs. Two injection schemes were followed for imbibition: displacement of H<sub>2</sub> with H<sub>2</sub>-equilibrated brine and with non-H<sub>2</sub>-equilibrated brine. The results from the two cycles were compared with each other.

**Findings:** The sandstone was found to be wetting to the brine and non-wetting to H<sub>2</sub> after both displacement cycles, with average contact angles of 54° and 53° for H<sub>2</sub>-equilibrated and non-H<sub>2</sub>-equilibrated brine respectively. We also found a higher recovery of H<sub>2</sub> (43.1%) when displaced with non-H<sub>2</sub>-

\* Corresponding author.

E-mail addresses: [zj21@hw.ac.uk](mailto:zj21@hw.ac.uk) (Z. Jangda), [h.menke@hw.ac.uk](mailto:h.menke@hw.ac.uk) (H. Menke), [a.busch@hw.ac.uk](mailto:a.busch@hw.ac.uk) (A. Busch), [s.geiger@tudelft.nl](mailto:s.geiger@tudelft.nl) (S. Geiger), [tom.bultreys@ugent.be](mailto:tom.bultreys@ugent.be) (T. Bultreys), [h.lewis@hw.ac.uk](mailto:h.lewis@hw.ac.uk) (H. Lewis), [k.singh@hw.ac.uk](mailto:k.singh@hw.ac.uk) (K. Singh).

equilibrated brine compared to that of H<sub>2</sub>-equilibrated brine (31.6%), indicating potential dissolution of H<sub>2</sub> in the unequilibrated imbibing brine at reservoir conditions. Our results suggest that underground H<sub>2</sub> storage may indeed be a suitable strategy for energy storage, but considerable further research is needed to fully comprehend the pore-scale interactions at reservoir conditions.

© 2022 The Author(s). Published by Elsevier Inc. This is an open access article under the CC BY license (<http://creativecommons.org/licenses/by/4.0/>).

## 1. Introduction

The Intergovernmental Panel on Climate Change (IPCC) [1] has warned that the world is set to reach the 1.5 °C warming level within the next two decades, and that only the most drastic and immediate cuts in carbon emissions will prevent an environmental disaster. Clean energy alternatives such as H<sub>2</sub> have the potential to support near-zero greenhouse gas emissions [2–7]. While there has been an unprecedented economic and political momentum towards the use of green H<sub>2</sub>, the large volumes needed for future demand would require new storage facilities [8–12].

Underground H<sub>2</sub> storage, for example in porous rocks or salt caverns [13–16], can provide an effective solution for short- and long-term storage to meet the fluctuations in energy demand. Salt caverns have already been used for storing natural gas and H<sub>2</sub>, for example, in Cheshire, Teesside, and Yorkshire [17] in the UK; however, they have a limited storage capacity [13] (170 TWh for all of Europe) [16]. An underground H<sub>2</sub> storage capacity between 250 and 1000 TWh is required for Europe by 2050, to support the forecasted demand of 2500 TWh [16]. To scale up the storage capacity, porous geological formations located deep underground, for example, containing depleted gas reservoirs [16,18,19] and saline aquifers, have the potential to provide the required storage volumes for H<sub>2</sub> (750 TWh capacity available in Europe) [16]. The feasibility of storing, and subsequently withdrawing H<sub>2</sub> repeatedly from such porous underground reservoirs to meet fluctuations in energy demand is currently being investigated in many countries [10,12,16,17,20].

Storage in subsurface reservoirs is regarded as economically viable, requiring substantially less capital cost and a lower levelized cost of H<sub>2</sub> storage (1.23–1.26 \$/kg) compared to salt caverns (1.61 \$/kg) [21]. However, there are significant uncertainties in storing H<sub>2</sub> in porous geological formations [22,23], which are due to the limited knowledge to predict and mitigate the negative effects of: (i) the uncontrolled migration and unwanted trapping of H<sub>2</sub> in reservoir rocks [23–25], (ii) H<sub>2</sub> reactivity with water and minerals [26–28], (iii) H<sub>2</sub> diffusion through the reservoir and caprock [8,29], and (iv) formation of biofilms [30,31] and their impacts on pore blockage and storage efficiency. All these are major challenges associated with underground H<sub>2</sub> storage and need to be studied independently in detail to obtain quantitative information of the contribution of each process on the effectiveness of H<sub>2</sub> storage in the subsurface.

Similar to other fluid–fluid displacement processes such as CO<sub>2</sub>-brine and CH<sub>4</sub>-brine, capillary trapping and wettability are of importance to H<sub>2</sub>-brine systems [32], as the amount of fluid trapping directly affects recovery efficiency [33–35]. The cyclic nature of an underground H<sub>2</sub> storage system renders these phenomena (capillary trapping and wettability) even more critical due to the repeated occurrence of drainage and imbibition cycles.

Capillary trapping mechanisms have been extensively studied for CO<sub>2</sub>, N<sub>2</sub>, and oil in various porous media [36–43]. These studies generally focus on the pore-scale, where the capillary trapping can be observed and quantified directly. However, it is not yet known if H<sub>2</sub> behaves similarly in subsurface rocks, in which capillary, viscous, and buoyancy forces have the potential to play a key role along with other geochemical and biological processes. Most of

the available studies on H<sub>2</sub> storage in rocks are focused on reservoir-scale numerical simulations [15,44–47], which do not yet provide pore-scale information.

In addition, there is still a lack of consensus on the wettability state for subsurface H<sub>2</sub> storage systems. First experimental studies have reported a wide range of contact angle values for H<sub>2</sub>-brine systems: using the tilted plate technique, contact angles of 0° to 50° for pure quartz and 50° to 70° for a quartz sample aged with stearic acid were measured for a pressure range of 1 to 250 bar and a temperature range of 20 to 70 °C [35]. A clear correlation between increasing contact angle and increasing pressure and temperature was observed. It was also reported [26] that aging rock samples in stearic acid increased the contact angles for H<sub>2</sub>-brine system from strongly water-wet to intermediate-wet for rocks containing calcite, dolomite and shale and, from strongly to weakly water-wet for rocks containing gypsum, quartz and basalt. The measurements were performed using the captive-bubble method for temperature ranges of 20 to 80 °C and pressure ranges of 10 to 100 bar. These studies conclude that under subsurface conditions, H<sub>2</sub> wettability is prone to be intermediate-wet for storage in depleted oil reservoirs.

In contrast, contact angle values between 21.1° and 43° have been reported for experiments performed on Berea and Bentheimer sandstone samples using the captive bubble method for temperature ranges of 20 to 50 °C and pressure ranges of 20 to 100 bar [24]. The contact angle was not affected by the changes in temperature, pressure, salinity, and rock type; however, it was affected by the bubble size. Similarly, advancing contact angles ranging between 13° to 39° and receding contact angles between 6° to 23° have been reported for a H<sub>2</sub>-water system using a microfluidic device with varying channel widths at a temperature of 20 °C and pressure of 10 bar [48]. Moreover, contact angles of 21.56° and 34.9° at two different experimental conditions of 50 bar and 20 °C, and 100 bar and 45 °C, respectively were reported based on core flood experiments in Voges sandstone [49]. These studies indicate strong water-wet conditions under all the tested parameters. However, to date no study has measured *in situ* contact angles of H<sub>2</sub>-brine systems at subsurface pressure and temperature conditions in a real rock.

*In situ* measurements have been made possible by using X-ray micro-tomography to visualize multiphase fluid displacement events at the pore-scale within porous media [41,50–54]. The images and measurements obtained using this technique have contributed towards developing more efficient strategies for hydrocarbon recoveries and underground CO<sub>2</sub> storage [36,40]. Recent studies have started to use this technology to investigate the pore-scale behavior [33,55] (wettability and trapping) of H<sub>2</sub>; however, these studies have been conducted at ambient conditions but not yet at representative subsurface storage conditions. The impact of changes in H<sub>2</sub> properties between ambient and reservoir conditions, such as changes in H<sub>2</sub> solubility in water as a function of pressure and temperature, requires experimental verification to provide an indication of expected fluid behavior during underground H<sub>2</sub> storage.

In this study, we have hence performed a cyclic H<sub>2</sub> core-flood experiment in a sandstone sample at temperature and pressure conditions of 50 °C and 100 bar respectively using a custom-

designed flow apparatus, and imaged the core *in situ* in an X-ray micro-CT scanner. The sample was imaged before and after drainage and imbibition, followed by segmentation and image analysis to quantify the phase volumes,  $H_2$  saturation, trapping, and contact angles. We provide a quantitative analysis of the amount of  $H_2$  trapped in the subsurface during underground  $H_2$  storage and determine contact angles *in situ*. Furthermore, we examine the potential effect of dissolution of  $H_2$  by providing a comparison of the residual  $H_2$  saturations when using  $H_2$ -equilibrated brine and non- $H_2$ -equilibrated brine as the imbibing fluid.

## 2. Materials and methods

### 2.1. Equipment and materials

A water-wet Bentheimer sandstone (typical composition of Quartz: 91.7%, Feldspar: 4.86%, Clay: 2.68%, Pyrite and Iron Hydroxides: 0.17%) [56] sample with a diameter of 6 mm and a length of 27 mm was used as the porous medium. Bentheimer sandstone is a well-characterized texturally homogeneous rock,

known to be water-wet with high porosity (20 to 26%) [56–58] and permeability (0.52 to 3.54 Darcy or  $5.13 \times 10^{-13}$  to  $3.49 \times 10^{-12}$  m<sup>2</sup>) [56], making it a suitable candidate to initiate the first investigations for pore-scale  $H_2$ -brine-rock interactions at reservoir conditions that can be visualized using a micro-CT scanner. The sample's permeability to water was measured separately and found to be 2.9 Darcy ( $2.86 \times 10^{-12}$  m<sup>2</sup>).

Before starting the flow experiment, the sample was immersed in methanol under a fume-hood for 12 h, and then dried in a vacuum oven under vacuum and at 100 °C for 18 h. A solution of 4 wt% potassium iodide (KI) salt (Sigma–Aldrich, UK) in deionized water (Thermo Scientific™ Barnstead™ LabTower™ TII Water Purification System) was used as the aqueous phase, which provided an effective X-ray contrast between brine (wetting phase) and  $H_2$  (non-wetting phase). High purity (>99.99%)  $H_2$  gas (BOC) was used as the gas (non-wetting) phase.

The experiment was performed using the flow apparatus shown in Figure S1 (Supplementary Material). It consists of a custom-designed high-pressure and high-temperature PEEK core holder

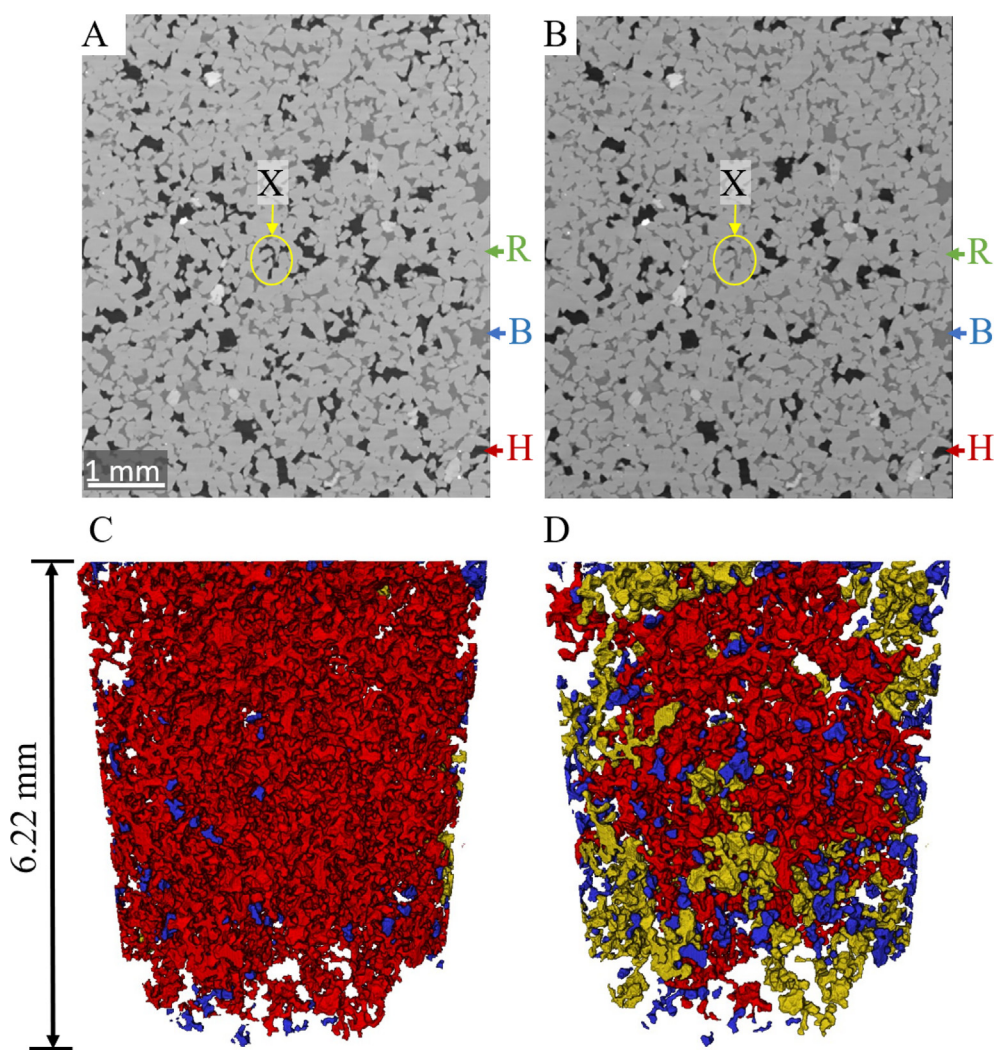


**Fig. 1.** 2D and 3D visualization of fluid distributions after drainage with  $H_2$  and imbibition with  $H_2$ -equilibrated brine. (A) 2D vertical cross-section of the filtered image after drainage, (B) 2D vertical cross-section of the filtered image after imbibition, (C) 3D visualization of  $H_2$  after drainage and (D) 3D visualization of  $H_2$  after imbibition. The 2D images show that after imbibition, the brine 'B' replaces  $H_2$  'H' in the smaller pores (see for example the pore space inside the yellow marking represented by 'X'), while  $H_2$  remains in the larger pores. 'R' represents the rock grains. The 3D images show that the connected  $H_2$  phase after drainage is fragmented into several  $H_2$  ganglia after imbibition. Red, yellow, and blue colours respectively indicate  $H_2$  ganglia occupying pores of sizes that are more than 100 times, between 10 and 100 times, and up to 10 times larger than the average pore size. (For interpretation of the references to colour in this figure legend, the reader is referred to the web version of this article.)



(rs systems), four high-pressure pumps (ISCO, three model 500D, and one model 100DX), and a reactor (Parr Instruments Company). The sample was wrapped with Teflon tape and aluminum foil and placed inside a Viton sleeve connected to the flow lines. The core holder was wrapped with a heating tape and securely fitted on top of the rotation stage of the X-ray micro-CT scanner (EasyTom 150, RX Solutions).

A thermocouple was inserted through one of the ports from the base of the core holder and attached outside the Viton sleeve with aluminum tape to measure the temperature outside the rock sample. To prevent the overheating of the system, another thermocouple was attached to the heating tape wrapped around the core holder. Four high-precision syringe pumps were used to apply confining pressure, and to inject and receive the fluids. A Hastelloy reactor was included in the flow loop to pre-equilibrate the brine with H<sub>2</sub> for 24 h at the experimental pressure and temperature conditions. The reactor was filled with brine up to 95% of its volume, with the remaining volume being H<sub>2</sub>. The fluids in the reactor were then heated to 50 °C and mixed using an entrainment stirrer until equilibrated while an ISCO pump provided a constant back pressure and a reservoir of H<sub>2</sub> gas. The equilibrated H<sub>2</sub> and brine were then pulled from the reactor's cell and through the core using the receiving pump. This pre-equilibration of fluids was carried out to avoid any possible dissolution of H<sub>2</sub> in the imbibing brine during injection in cycle 1 (discussed in the forthcoming section).

## 2.2. Experimental methodology

The experimental protocol consisted of the following steps:

- i. loaded the sample into the core holder;
- ii. applied a confining pressure of 20 bar around the sample with deionized water;
- iii. flushed the sample with CO<sub>2</sub> from the base of the sample to displace any air inside the sample;
- iv. injected 75 pore volumes (PV) (where, 1 PV = 0.19 mL) of non-H<sub>2</sub>-equilibrated brine from the base of the sample at a flow rate of 0.5 mL·min<sup>-1</sup>, ensuring 100% brine saturation;
- v. switched on the heating to gradually increase the temperature of the flow system to 50 °C in one hour;

- vi. pressurised the flow system with non-H<sub>2</sub>-equilibrated brine in steps of 10 bar each, while maintaining a 20 bar difference between the pore and the confining fluid pressures, to reach a pore pressure of 100 bar and a confining pressure of 120 bar;
- vii. injected 70 PV of H<sub>2</sub>-equilibrated brine from the reactor to completely displace non-H<sub>2</sub>-equilibrated brine from the sample;
- viii. started cycle 1 and injected 15 PV of H<sub>2</sub> (non-wetting phase) from the reactor to commence the first drainage cycle at a flow rate of 0.05 mL·min<sup>-1</sup> ensuring a capillary number (Ca) of  $4.2 \times 10^{-9}$ . Here,  $Ca = \frac{\mu V}{\gamma}$ , where  $\mu$  is the H<sub>2</sub> viscosity ( $9.64 \times 10^{-6}$  Pa·s) [59],  $V$  is the velocity of the injected fluid (H<sub>2</sub>) and  $\gamma$  is the interfacial tension (0.0683 Nm<sup>-1</sup>) [60] between H<sub>2</sub> and water at the experimental conditions. In this step, H<sub>2</sub> was injected from the top of the sample;
- ix. injected 5 PV of H<sub>2</sub>-equilibrated brine (wetting phase) from the reactor to displace H<sub>2</sub> at the same flow rate ensuring a Ca of  $2.3 \times 10^{-6}$ . In this step, brine was injected from the base of the sample. The sample was scanned after leaving it overnight and it showed complete removal of H<sub>2</sub> from the pore space, which could be due to diffusion of H<sub>2</sub> through the Viton sleeve into the confining water along minute and microscopically undetectable channels in the wrapping of the core sample;
- x. started cycle 2 by repeating step viii, i.e., injected 15 PV of H<sub>2</sub> from the top of the sample to commence the second drainage cycle with the same Ca of  $4.2 \times 10^{-9}$  as the first drainage cycle.
- xi. injected 5 PV of non-H<sub>2</sub>-equilibrated brine (wetting phase) from the base of the sample using a pump with the same Ca of  $2.3 \times 10^{-6}$  as the first imbibition cycle.

The central vertical section of the sample, which had a length of 6.7 mm, was X-ray scanned after step (ii) to image the dry sample, and immediately after drainage or imbibition in steps (viii) to (xi) to visualize the fluids after each displacement process. All scans were acquired using an EasyTom 150 X-ray micro-CT machine. The scans were acquired with a voxel size of 5 μm and with

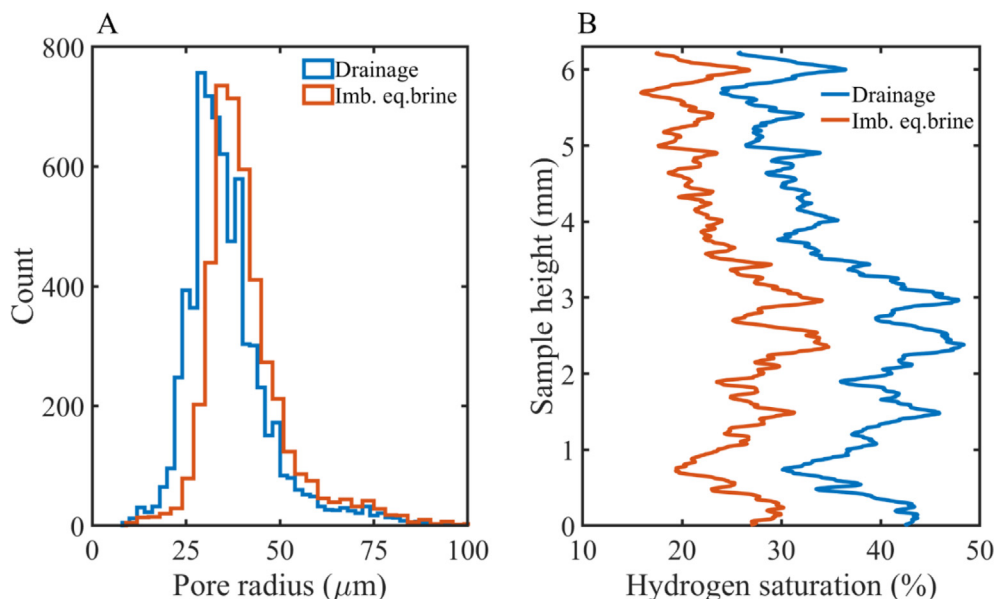


**Fig. 2.** H<sub>2</sub> pore occupancy and saturation profiles. (A) Radius of the pores occupied by H<sub>2</sub> after drainage with H<sub>2</sub> and imbibition with H<sub>2</sub>-equilibrated brine and (B) H<sub>2</sub> saturation profile along the height of the sample after drainage with H<sub>2</sub> and imbibition with H<sub>2</sub>-equilibrated brine.

1792 projections. The tube voltage was 90 kV and the X-ray tube power was 10 W. The duration of each scan was 2 h.

### 2.3. Image processing

The raw data from each scan was reconstructed using the Easy-Tom Xact software. The resulting images were then processed and visualized using Avizo 2021.2 (ThermoFisher Scientific) as shown in Figure S2 (Supplementary Material). A cylindrical mask was applied on the reconstructed data to remove the regions outside the core sample including the Viton sleeve, aluminum foil and Teflon tape wrapped around the sample. A sub-volume of 1250 slices corresponding to a sample length of 6.22 mm was selected for image processing, on which a non-local means filter [61] was applied to remove the noise. All wet images (containing H<sub>2</sub> and brine) were registered to the dry reference image and then resampled onto the same voxel grid as used in the dry reference image. Image segmentation was then performed using a watershed algorithm [62] based on the grayscale intensity of each voxel. The dry sample was segmented into pores and grains which served

as the mask for the wet segmented images. The porosity value of 22.8% obtained from the segmented volume is in good agreement with reported Bentheimer porosity values between 20 and 26% [57,58]. The image segmentation workflow for wet scans (with fluids) is detailed in Figure S3 (Supplementary Material), and the grayscale histograms for the raw and filtered images are shown in Figures S4 to S8 (Supplementary Material).

### 2.4. Saturation, pore occupancy and contact angle

Quantitative analysis was then performed on the segmented images to calculate H<sub>2</sub> saturations, pore occupancy, and contact angles. H<sub>2</sub> phase volume after each displacement process was used to calculate the initial and residual saturations. To obtain the H<sub>2</sub> pore occupancy after each displacement process, first the pores from the dry scan were extracted using a network extraction algorithm [63]. The algorithm employs the modified maximal ball algorithm that extracts simplified networks of pores and throats [64], by finding constrictions and wider regions in the pore space and hence identifies where pores in the image are separated by throat

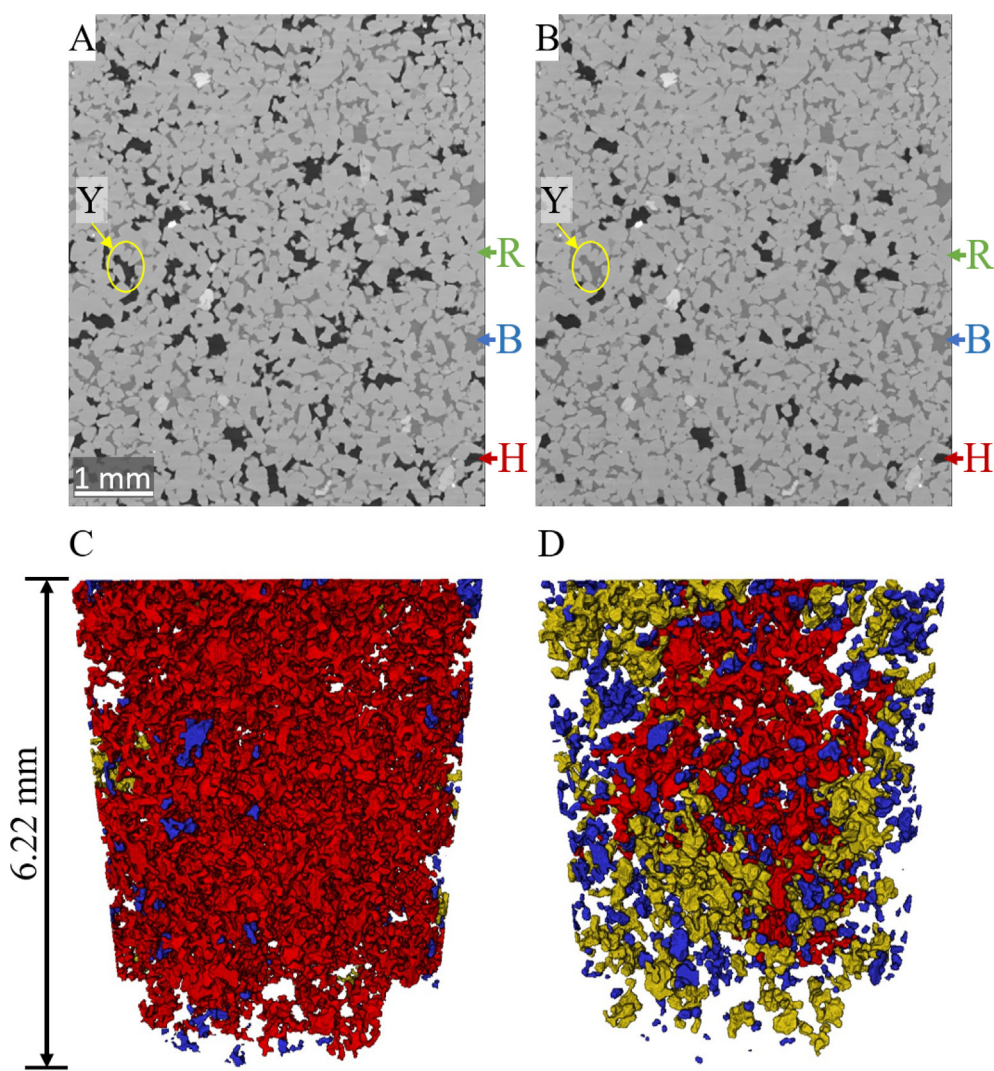


**Fig. 3.** 2D and 3D visualization of fluid distributions after drainage with H<sub>2</sub> and imbibition with non-H<sub>2</sub>-equilibrated brine. (A) 2D cross-section of the filtered image after drainage, (B) 2D cross-section of the filtered image after imbibition. (C) 3D visualization of H<sub>2</sub> after drainage and (D) 3D visualization of H<sub>2</sub> after imbibition. The 2D images show that after imbibition, the brine 'B' replaces H<sub>2</sub> 'H' even in some of the pores (see for example the pore space inside the yellow circles represented by 'Y') which remained saturated with H<sub>2</sub> after imbibition with H<sub>2</sub>-equilibrated brine (compared with Fig. 1B). 'R' represents the rock grains. The 3D images show that the connected H<sub>2</sub> phase after drainage is fragmented into several H<sub>2</sub> ganglia after imbibition. (For interpretation of the references to colour in this figure legend, the reader is referred to the web version of this article.)

surfaces [65]. The extracted network statistics are provided in Table S1 (Supplementary Material). The pores (extracted as spheres from the network) were then overlaid on each of the segmented H<sub>2</sub> image, to determine the radii and the number of pores filled with H<sub>2</sub> after each displacement process.

To identify the wettability of the system after each imbibition step, we measured the H<sub>2</sub>/brine/rock contact angles on each voxel at the three-phase contact line on a sub-volume of 2.5 mm<sup>3</sup> using an automated algorithm [66] with a low standard deviation ( $\sigma$  of 8 and 12 for the two experimental datasets) [66]. This method has been used in multiple studies [67–71] to automatically measure contact angle values for X-ray tomography images with reasonable accuracy. However, using this *in situ* algorithm at the current image resolution, there is a possibility of some error related to voxel resolution at the three-phase contact line [33].

### 3. Results and discussion

#### 3.1. Drainage and imbibition cycle 1 (H<sub>2</sub>-equilibrated brine)

The imaging results of H<sub>2</sub> drainage and imbibition with pre-equilibrated brine are shown in Fig. 1. The filtered 2D vertical cross-sections in Fig. 1A and B show the displacement of H<sub>2</sub> with brine, predominantly in the smaller pores after imbibition. Fig. 1C shows a well-connected percolating H<sub>2</sub> cluster (red) with a few isolated H<sub>2</sub> ganglia shown in blue and yellow. During imbibition, H<sub>2</sub> fragments into smaller clusters (Fig. 1D). The colours in Fig. 1C and D represent the different sizes of the H<sub>2</sub> ganglia classified based on the average pore size ( $\hat{S}$ ) of  $1.12 \times 10^6 \mu\text{m}^3$ , where

- Red – H<sub>2</sub> ganglia occupying pore sizes 100 times larger than  $\hat{S}$
- Yellow – H<sub>2</sub> ganglia occupying pore sizes 10 to 100 times larger than  $\hat{S}$
- Blue – H<sub>2</sub> ganglia occupying pore sizes smaller than 10 times  $\hat{S}$

The H<sub>2</sub> saturation calculated after drainage was 36.3%, which reduced to 24.8% after imbibition with H<sub>2</sub>-equilibrated brine, giving a recovery of 31.6%.

The H<sub>2</sub> pore occupancy is shown in Fig. 2A. The shift of H<sub>2</sub> pore occupancy towards larger pores indicates that the larger pores are preferentially occupied by trapped H<sub>2</sub> after imbibition. The average pore radius of the pores occupied by H<sub>2</sub> increases from 36  $\mu\text{m}$  ( $\sigma$  of 11  $\mu\text{m}$ ) after drainage to 41  $\mu\text{m}$  ( $\sigma$  of 12  $\mu\text{m}$ ) after imbibition. The H<sub>2</sub> saturation profile along the height of the sample is plotted in Fig. 2B. The saturation varies between 24% and 48% during drainage and 15% and 35% during imbibition, showing some heterogeneity in the sample. Furthermore, the change in saturation between drainage and imbibition remains constant over the length of the visualized subsection, indicating the absence of capillary end effects. The absence of capillary end effects was expected as only a 6.2 mm long central section of the 27 mm core sample is analysed.

#### 3.2. Drainage and imbibition cycle 2 (non-H<sub>2</sub>-equilibrated Brine)

The pore occupancy for cycle 2 after drainage with H<sub>2</sub> and imbibition with non-H<sub>2</sub>-equilibrated brine is shown in Fig. 3. The filtered 2D vertical cross-sections in Fig. 3A and B show that brine displaced H<sub>2</sub> in a larger number of pores compared to cycle 1. Like cycle 1, H<sub>2</sub> mostly exists as a single cluster after drainage (Fig. 3C) which is then fragmented into smaller clusters during imbibition (Fig. 3D). The colours in Fig. 3 represent H<sub>2</sub> ganglia occupying pores of different sizes classified based on an  $\hat{S}$  value of  $1.12 \times 10^6 \mu\text{m}^3$  using the same colour classification scheme as for cycle 1 discussed above.

The H<sub>2</sub> saturation after drainage was 35.8%. The residual H<sub>2</sub> saturation after imbibition with non-H<sub>2</sub>-equilibrated brine was 20.4%, indicating a recovery of 43.1%. However, we posit that it is likely that some of the H<sub>2</sub> dissolved in the non-H<sub>2</sub>-equilibrated brine resulting in lower residual saturation in this cycle. Moreover, isolated clusters of H<sub>2</sub> in Fig. 3D appear visually different than those in Fig. 1D, which will be compared quantitatively in the forthcoming sections.

Fig. 4A shows the pore occupancy of H<sub>2</sub> calculated using image analysis for both drainage and imbibition in cycle 2. We observe the same shift as in cycle 1, that is larger pores remained occupied by H<sub>2</sub> after imbibition. The average radii of the pores occupied by H<sub>2</sub> are 36  $\mu\text{m}$  ( $\sigma$  of 12  $\mu\text{m}$ ) after drainage, and 43  $\mu\text{m}$  ( $\sigma$  of 12  $\mu\text{m}$ ) after imbibition. These values are similar to the values

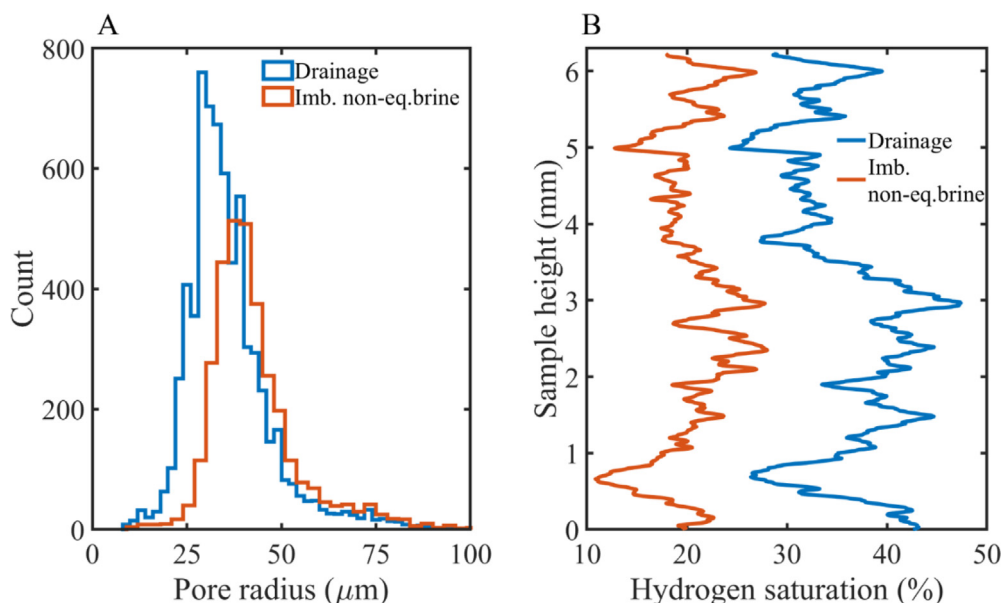


Fig. 4. H<sub>2</sub> pore occupancy and saturation profiles. (A) Radius of the pores occupied by H<sub>2</sub> after drainage with H<sub>2</sub> and imbibition with non-H<sub>2</sub>-equilibrated brine and (B) H<sub>2</sub> saturation profile along the height of the sample after drainage with H<sub>2</sub> and imbibition with non-H<sub>2</sub>-equilibrated brine.



obtained after cycle 1; however, the reduction in the number of pores occupied by  $H_2$  after imbibition is much higher. This difference shows that although  $H_2$  still preferentially occupies the larger pores after imbibition, the number of pores occupied by  $H_2$  is significantly lower, again indicating possible dissolution of  $H_2$  in the imbibing brine. The  $H_2$  saturation profile along the height of the sample is shown in Fig. 4B. The saturation varies between 24% and 47% during drainage and 10% and 28% during imbibition. The change in saturation between drainage and imbibition is larger than in cycle 1, indicating a greater loss of  $H_2$ . However, this change is still constant over the length of the sample.

### 3.3. Comparison between cycles

Fig. 5A shows a comparison of the  $H_2$  saturation along the height of the sample for drainage cycles 1 and 2, while Fig. 5B shows the  $H_2$  pore occupancy. We observe very little difference between the two drainage cycles, indicating a repeatability of the experimental protocol for drainage. Both, the qualitative and quan-

titative analysis show that the two drainage steps are similar compared to the two imbibition steps.

The average pore radii and the number of pores occupied by  $H_2$  after both drainage cycles (6889 after drainage 1 and 6756 after drainage 2) are similar. The saturation profiles are also similar for both cycles (Fig. 5A). However, we observe significant differences between cycle 1 and 2 for imbibition (Fig. 5C). The residual  $H_2$  saturation in cycle 2 is lower compared to cycle 1, especially in the bottom part of the sample. This difference may indicate that during imbibition in cycle 2, some  $H_2$  dissolves into the brine near the inlet, lowering the residual  $H_2$  saturation in that part of the sample. As the non- $H_2$ -equilibrated brine travels further into the sample, the brine starts to get equilibrated with  $H_2$  and dissolves less  $H_2$  in the upper part of the sample. The saturation profile then starts to align with the saturation profile during the imbibition step of cycle 1. The pore occupancy profiles for  $H_2$  (Fig. 5D) for both imbibition steps are similar in terms of the preferred size of pores occupied by  $H_2$ ; however, the number of occupied pores (3331) is significantly lower in the case of imbibition with non- $H_2$ -equilibrated brine, compared to 4333 for imbibition with  $H_2$ -

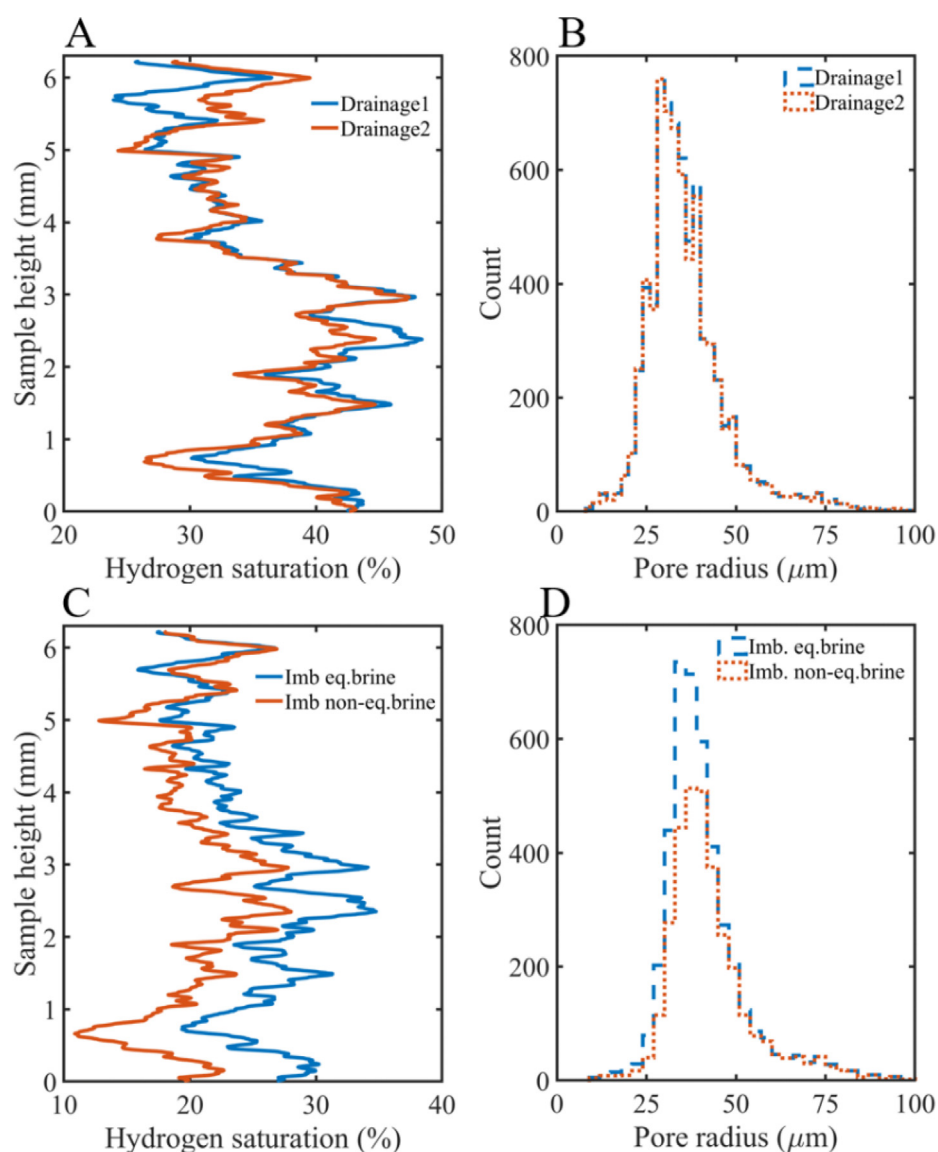


**Fig. 5.**  $H_2$  saturation profiles and pore occupancy distributions. (A)  $H_2$  saturation profile along the height of the sample after the two drainage steps, (B) Radius of the pores occupied by  $H_2$  after the two drainage steps, (C)  $H_2$  saturation profile along the height of the sample after imbibition with 5 PV of  $H_2$ -equilibrated brine and 5 PV of non- $H_2$ -equilibrated brine, and (D) Radius of the pores occupied by  $H_2$  after imbibition with 5 PV of  $H_2$ -equilibrated brine and 5 PV of non- $H_2$ -equilibrated brine.



equilibrated brine, which is expected considering the lower residual saturation that was observed.

Image analysis also shows that imbibition with non-H<sub>2</sub>-equilibrated brine (in cycle 2) resulted in brine occupying pores which remained filled with H<sub>2</sub> in the previous imbibition (in cycle 1) as shown in Fig. 6. Although the solubility of H<sub>2</sub> in water is low (~0.001 g.kg<sup>-1</sup> at the experimental conditions [72]), due to the small size of H<sub>2</sub> molecules, the mass of H<sub>2</sub> occupying the pore space is small. Hence, up to 7% of the H<sub>2</sub> present in the pores during the injection of 5 PV of non-H<sub>2</sub>-equilibrated brine could potentially dissolve. This dissolution could explain the lower residual saturation after imbibition with non-H<sub>2</sub>-equilibrated brine.

### 3.4. Comparison of fluid saturations

Quantification of fluid saturations using *in situ* X-ray flow visualization experiments has been frequently reported in the literature for CO<sub>2</sub>, N<sub>2</sub>, and oil-brine systems. Some of the earlier reported studies for CO<sub>2</sub>-brine systems on sandstone samples [37,40,73–75] are plotted in Fig. 7 and compared with our results.

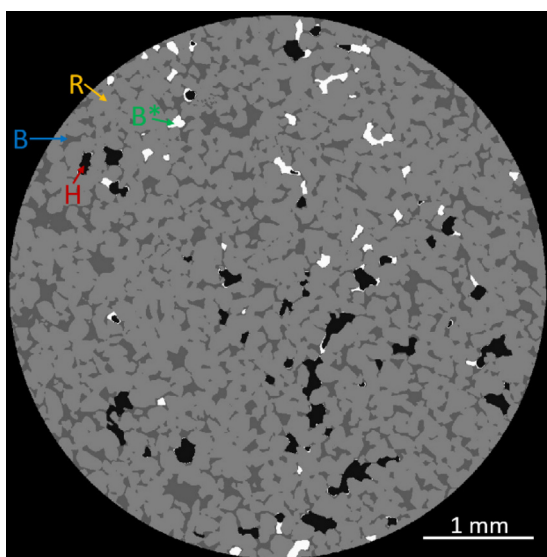


Fig. 6. 2D X-ray CT image after imbibition with non-H<sub>2</sub>-equilibrated brine. The bright spots (B\*) highlight pore spaces that were filled with brine after imbibition with non-H<sub>2</sub>-equilibrated brine in cycle 2, which were occupied by H<sub>2</sub> after imbibition with H<sub>2</sub>-equilibrated brine in cycle 1.

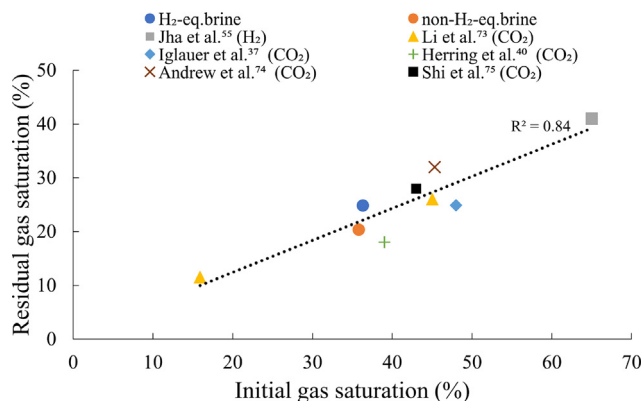


Fig. 7. Initial and residual H<sub>2</sub> saturations for the two imbibition steps in this study compared with literature data for H<sub>2</sub> and CO<sub>2</sub> obtained from X-ray flow visualization experiments.

Four of these earlier studies [37,73–75] are at experimental conditions similar to those used in this work and the recovery trends are qualitatively similar. Interestingly, the initial and residual saturation values of CO<sub>2</sub> closest to our results are for the reported values at ambient conditions (with CO<sub>2</sub> as the gaseous phase) [40]. This could be due to the relatively smaller difference in the density of H<sub>2</sub> at the temperature and pressure used in our experiment and CO<sub>2</sub> at ambient conditions, compared to CO<sub>2</sub> at high temperatures and pressures.

Recent experimental measurements for H<sub>2</sub> saturation in a H<sub>2</sub>-brine system [55] at ambient conditions are also plotted in Fig. 7. In this experiment, an initial H<sub>2</sub> saturation of 64% and a residual H<sub>2</sub> saturation of 41% after 5 PV of brine injection was reported for a Gosford sandstone [55]. Although the recovery trend of our results broadly agrees with this work, the reported initial and residual H<sub>2</sub> saturation values are significantly different from our results. This difference could be due to the higher temperature and pressure conditions and a larger sub-volume analysed in our work, which provides a more realistic scenario for subsurface storage.

Additionally, the decrease in H<sub>2</sub> residual saturation due to dissolution of H<sub>2</sub> in the non-H<sub>2</sub>-equilibrated brine is likely to be an important parameter for reservoir-scale modelling, especially during cyclic injection of H<sub>2</sub>. The initial recovery from the first injection into the reservoir may be low with subsequent cycles producing more H<sub>2</sub> as the reservoir brine is slowly equilibrated and loss of H<sub>2</sub> gas due to dissolution and trapping decreases. The impact of dissolution and other important factors like microbial activity and diffusion on the fluid saturations during underground H<sub>2</sub> storage warrants further investigations.

### 3.5. Contact angle

Contact angles were determined for a 2.5 mm<sup>3</sup> sub-volume for each imbibition step. The results (Fig. 8) show water-wet conditions with an average contact angle (measured through brine) of 54° after imbibition with H<sub>2</sub>-equilibrated brine (cycle 1) and 53° after imbibition with non-H<sub>2</sub>-equilibrated brine (cycle 2). These contact angle values agree with the measurements performed using multiple methods on a H<sub>2</sub>-brine system in a Bentheimer sandstone [33], where average contact angles were reported to be in the range 39.8° to 59.8°. The mean contact angle (59.8°), which was obtained via the same 3D local method [66] used in our study, agrees well with our results. Other studies [24,48,49]

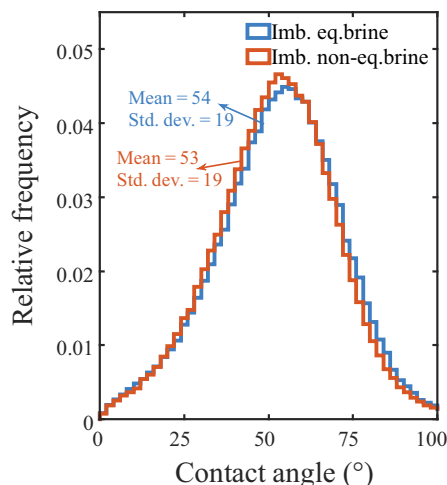


Fig. 8. Contact angle distributions after imbibition with H<sub>2</sub>-equilibrated brine (cycle 1) and non-H<sub>2</sub>-equilibrated brine (cycle 2).

have found sandstone samples to be strongly water-wet for H<sub>2</sub>-brine systems. They have reported contact angles between 6° and 43° regardless of the tested parameters for temperatures between 20 °C and 50 °C and pressures between 20 bar and 100 bar.

#### 4. Conclusion

In this study we have imaged the spatial distribution and trapping of H<sub>2</sub> after the injection of both H<sub>2</sub>-equilibrated and non-H<sub>2</sub>-equilibrated brine in a Bentheimer sandstone at subsurface pressure and temperature conditions. The analysis shows that the rock sample is water-wet at subsurface conditions with an average contact angle of 54° and 53° obtained after H<sub>2</sub>-equilibrated and non-H<sub>2</sub>-equilibrated brine injection, respectively. These observations are in agreement with some of the recent experimental studies [33,35]. Other studies [24,48,49] have also reported strongly water-wet conditions for H<sub>2</sub>-brine systems. These water-wet conditions can enhance snap-off processes resulting in more trapping of H<sub>2</sub> [76]. The robust determination of wettability is hence key to understanding and quantifying trapping and recovery. More *in situ* experimental datasets are needed for different pressure and temperature conditions as well as rock types and flow rates to understand how the pore-scale displacement processes impact large-scale H<sub>2</sub> storage.

Our analysis presents new insights into the possible dissolution of H<sub>2</sub> into brine at subsurface conditions. The results show a decrease in residual H<sub>2</sub> saturation and a decrease in H<sub>2</sub> pore occupancy when the sample was imbibed with non-H<sub>2</sub>-equilibrated brine, indicating that dissolution of H<sub>2</sub> may be an important consideration for the accurate prediction of H<sub>2</sub> recovery. Since *in situ* experimental work on H<sub>2</sub> at high temperature and pressure conditions is still scarce, this effect was not reported in any previous work but can be a critical aspect to consider for future research.

We have found that the trend in recovery factor for our experiment is consistent with previously reported observations [37,73–75] for supercritical CO<sub>2</sub>-brine experiments at similar pressure and temperature conditions. However, the residual saturation values (corresponding to the initial saturation values) closest to our results are for CO<sub>2</sub>-brine experiment at ambient conditions [40].

In summary, even though porous geological formations containing depleted gas reservoirs or saline aquifers can provide large storage volumes for H<sub>2</sub>, pore-scale interactions at reservoir conditions need to be further investigated to provide the key physical insights if and why these porous reservoirs are suitable for long-term and cyclic underground storage. A key technique in this regard is utilizing fast synchrotron X-ray imaging [52,53,67,77] to obtain time-resolved 3D images for visualization and quantification of the dynamics of fluid displacement during H<sub>2</sub> injection and production.

#### Data availability statement

The raw, filtered and segmented tomographic datasets have been uploaded on a public repository (figshare), the details of which are provided in Ref [78], <https://doi.org/10.6084/m9.figshare.20260968.v1>.

#### CRediT authorship contribution statement

**Zaid Jangda:** Conceptualization, Methodology, Software, Formal analysis, Investigation, Data curation, Visualization. **Hannah Menke:** Methodology, Software, Formal analysis, Investigation, Visualization. **Andreas Busch:** Conceptualization, Methodology, Investigation. **Sebastian Geiger:** Conceptualization, Methodology, Investigation. **Tom Bultreys:** Software, Formal analysis. **Helen Lewis:** Methodology. **Kamaljit Singh:** Conceptualization, Method-

ology, Formal analysis, Investigation, Data curation, Supervision, Project administration.

#### Declaration of Competing Interest

The authors declare that they have no known competing financial interests or personal relationships that could have appeared to influence the work reported in this paper.

#### Acknowledgment

We gratefully acknowledge Jim Buckman, Clayton Magill, Paul Miller, Robert Loudon, Jim Allison, Emma Samson and Juliane Bischoff for their support in the preparation of the equipment and materials used for our experiment. We also thank Leila Hashemi, Maartje Boon, Hadi Hajibeygi, Gülce Kalyoncu, Mostafa Borji and Eike Marie Thaysen for valuable comments and discussion. We are thankful to Energi Simulation for providing partial funding for this research and The Digital Imaging Hub at the Institute of GeoEnergy Engineering, Heriot-Watt University for assisted access to their X-ray Tomography Facility.

#### Appendix A. Supplementary data

Supplementary data to this article can be found online at <https://doi.org/10.1016/j.jcis.2022.09.082>.

#### References

- [1] IPCC, *Climate Change 2022: Mitigation of Climate Change. Contribution of Working Group III to the Sixth Assessment Report of the Intergovernmental Panel on Climate Change*, Cambridge University Press, Cambridge, UK and New York, NY, USA, 2022, <https://doi.org/10.1017/9781009157926>. <https://www.ipcc.ch/report/ar6/wg3/>.
- [2] IEA, *The Future of Hydrogen*, IEA, Paris, 2019. <https://www.iea.org/reports/the-future-of-hydrogen>.
- [3] Climate Change Committee (CCC) *The Sixth Carbon Budget - The UK's path to Net Zero, 2020* <https://www.theccc.org.uk/publication/sixth-carbon-budget/>.
- [4] Scottish Government, *Scottish Hydrogen Assessment (2020)*. <https://www.gov.scot/publications/scottish-hydrogen-assessment-report/documents/>.
- [5] UK Government, *UK Hydrogen Strategy (2021)*. <https://www.gov.uk/government/publications/uk-hydrogen-strategy>.
- [6] *The Path Toward a Hydrogen Economy: How Industry Can Broaden the Use of Hydrogen*. <https://www.kapsarc.org/research/publications/the-path-toward-a-hydrogen-economy-how-industry-can-broaden-the-use-of-hydrogen/> (2020).
- [7] UK Parliament POSTNOTE. *Low-carbon hydrogen supply*. (2021).
- [8] S. Flesch, D. Pudlo, D. Albrecht, A. Jacob, F. Enzmann, *Hydrogen underground storage - Petrographic and petrophysical variations in reservoir sandstones from laboratory experiments under simulated reservoir conditions*, *Int. J. Hydrogen Energy* 43 (2018) 20822–20835.
- [9] D. Zivar, S. Kumar, J. Foroozesh, *Underground hydrogen storage: A comprehensive review*, *Int. J. Hydrogen Energy* 46 (2021) 23436–23462.
- [10] R. Tarkowski, *Underground hydrogen storage: Characteristics and prospects*, *Renew. Sustain. Energy Rev.* 105 (2019) 86–94.
- [11] N.S. Muhammed et al., *A review on underground hydrogen storage: Insight into geological sites, influencing factors and future outlook*, *Energy Rep.* 8 (2022) 461–499.
- [12] N. Heinemann et al., *Enabling large-scale hydrogen storage in porous media—the scientific challenges*, *Energy Environ. Sci.* 14 (2021) 853–864.
- [13] Netherlands Enterprise Agency. *“The effects of hydrogen injection in natural gas networks for the Dutch underground storages” Final Report Commissioned by the ministry of Economic Affairs*. (2017).
- [14] F. Johansson, J. Spross, R. Damasceno, D.J. Johansson, H. Stille, *Investigation of research needs regarding the storage of hydrogen gas in lined rock caverns: Prestudy for Work Package 2.3 in HYBRIT Research Program 1*. (2018).
- [15] W. Liu et al., *Feasibility evaluation of large-scale underground hydrogen storage in bedded salt rocks of China: A case study in Jiangsu province*, *Energy* 198 (2020) 117348.
- [16] A. Cavanagh, H. Yousefi, M. Wilkinson, R. Groenenberg, *HyUSPRe Hydrogen Underground Storage in Porous Reservoirs Hydrogen storage potential of existing European gas storage sites in depleted gas fields and aquifers The HyUSPRe consortium*. [www.hyuspre.eu](http://www.hyuspre.eu).
- [17] H.B.J. Stone, I. Veldhuis, R.N. Richardson, *Underground hydrogen storage in the UK*, *Geological Society, London, Special Publications* 313 (2009) 217–226.

- [18] M. Lysy, M. Fernø, G. Ersland, Seasonal hydrogen storage in a depleted oil and gas field, *Int. J. Hydrogen Energy* 46 (2021) 25160–25174.
- [19] A. Amid, D. Mignard, M. Wilkinson, Seasonal storage of hydrogen in a depleted natural gas reservoir, *Int. J. Hydrogen Energy* 41 (2016) 5549–5558.
- [20] J. Mouli-Castillo, N. Heinemann, K. Edlmann, Mapping geological hydrogen storage capacity and regional heating demands: An applied UK case study, *Appl. Energy* 283 (2021) 116348.
- [21] A.S. Lord, P.H. Kobos, D.J. Borna, Geologic storage of hydrogen: Scaling up to meet city transportation demands, *Int. J. Hydrogen Energy* 39 (2014) 15570–15582.
- [22] S.R. Thiyagarajan, H. Emadi, A. Hussain, P. Patange, M. Watson, A comprehensive review of the mechanisms and efficiency of underground hydrogen storage, *J. Storage Mater.* 51 (2022) 104490.
- [23] B. Pan, X. Yin, Y. Ju, S. Iglauer, Underground hydrogen storage: Influencing parameters and future outlook, *Adv. Colloid Interface Sci.* 294 (2021) 102473.
- [24] L. Hashemi, W. Glerum, R. Farajzadeh, H. Hajibeygi, Contact angle measurement for hydrogen/brine/sandstone system using captive-bubble method relevant for underground hydrogen storage, *Adv. Water Resour.* 154 (2021) 103964.
- [25] D.S. Mahdi, E.A. Al-Khdeawi, Y. Yuan, Y. Zhang, S. Iglauer, Hydrogen underground storage efficiency in a heterogeneous sandstone reservoir, *Adv. Geo-Energy Res.* 5 (2021) 437–443.
- [26] H. Esfandyari et al., Experimental evaluation of rock mineralogy on hydrogen-wettability: Implications for hydrogen geo-storage, *J. Storage Mater.* 52 (2022) 104866.
- [27] A. Al-Yaseri, D. Wolff-Boenisch, C.A. Fauziah, S. Iglauer, Hydrogen wettability of clays: Implications for underground hydrogen storage, *Int. J. Hydrogen Energy* 46 (2021) 34356–34361.
- [28] A. Hassanpouryouzband et al., Geological Hydrogen Storage: Geochemical Reactivity of Hydrogen with Sandstone Reservoirs, *ACS Energy Lett.* 7 (2022) 2203–2210.
- [29] Z. Bo, L. Zeng, Y. Chen, Q. Xie, Geochemical reactions-induced hydrogen loss during underground hydrogen storage in sandstone reservoirs, *Int. J. Hydrogen Energy* 46 (2021) 19998–20009.
- [30] E. Thaysen et al., Estimating Microbial Hydrogen Consumption in Hydrogen Storage in Porous Media as a Basis for Site Selection, *Renew. Sustain. Energy Rev.* 151 (2020) 111481.
- [31] N. Dopffel, S. Jansen, J. Gerritse, Microbial side effects of underground hydrogen storage – Knowledge gaps, risks and opportunities for successful implementation, *Int. J. Hydrogen Energy* 46 (2021) 8594–8606.
- [32] M. Boon, H. Hajibeygi, Experimental characterization of H<sub>2</sub>/water multiphase flow in heterogeneous sandstone rock at the core scale relevant for underground hydrogen storage (UHS), *Sci. Rep.* 12 (2022) 14604.
- [33] S. Higgs et al., In-situ hydrogen wettability characterisation for underground hydrogen storage, *Int. J. Hydrogen Energy* 47 (2022) 13062–13075.
- [34] M. Rücker et al., Workflow for Upscaling Wettability from the Nanoscale to Core Scale, *Petrophys. - SPWLA J. Formation Eval. Reservoir Descrip.* 61 (2020) 189–205.
- [35] S. Iglauer, M. Ali, A. Keshavarz, Hydrogen Wettability of Sandstone Reservoirs: Implications for Hydrogen Geo-Storage, *Geophys. Res. Lett.* 48 (2021) e2020GL090814.
- [36] A. Alhosani et al., Pore-scale mechanisms of CO<sub>2</sub> storage in oilfields, *Sci. Rep.* 10 (2020) 8534.
- [37] S. Iglauer, A. Paluszny, C.H. Pentland, M.J. Blunt, Residual CO<sub>2</sub> imaged with X-ray micro-tomography, *Geophys. Res. Lett.* 38 (2011) L21403.
- [38] S.J. Jackson, S. Krevor, Small-Scale Capillary Heterogeneity Linked to Rapid Plume Migration During CO<sub>2</sub> Storage, *Geophys. Res. Lett.* 47 (2020) e2020GL088616.
- [39] C.A. Reynolds, M.J. Blunt, S. Krevor, Multiphase Flow Characteristics of Heterogeneous Rocks From CO<sub>2</sub> Storage Reservoirs in the United Kingdom, *Water Resour. Res.* 54 (2018) 729–745.
- [40] A.L. Herring et al., Effect of fluid topology on residual nonwetting phase trapping: Implications for geologic CO<sub>2</sub> sequestration, *Adv. Water Resour.* 62 (2013) 47–58.
- [41] Y. Liu, H. Wang, Z. Shen, Y. Song, Estimation of CO<sub>2</sub> storage capacity in porous media by using X-ray micro-CT, *Energy Proc.* 37 (2013) 5201–5208.
- [42] C. Garing, M. Voltolini, J.B. Ajo-Franklin, S.M. Benson, Pore-scale Evolution of Trapped CO<sub>2</sub> at Early Stages Following Imbibition Using Micro-CT Imaging, *Energy Proc.* 14 (2017) 4872–4878.
- [43] S. Iglauer et al., Residual Trapping of CO<sub>2</sub> in an Oil-Filled, Oil-Wet Sandstone Core: Results of Three-Phase Pore-Scale Imaging, *Geophys. Res. Lett.* 46 (2019) 11146–11154.
- [44] K. Luboń, R. Tarkowski, Numerical simulation of hydrogen injection and withdrawal to and from a deep aquifer in NW Poland, *Int. J. Hydrogen Energy* 45 (2020) 2068–2083.
- [45] N. Hassannayebi, S. Azizmohammadi, M. de Lucia, H. Ott, Underground hydrogen storage: application of geochemical modelling in a case study in the Molasse Basin, Upper Austria, *Environ. Earth Sci.* 78 (2019) 177.
- [46] Z. Cai, K. Zhang, C. Guo, Development of a novel simulator for modelling underground hydrogen and gas mixture storage, *Int. J. Hydrogen Energy* 47 (2022) 8929–8942.
- [47] P. Gabrielli et al., Seasonal energy storage for zero-emissions multi-energy systems via underground hydrogen storage, *Renew. Sustain. Energy Rev.* 121 (2020) 109629.
- [48] W. van Rooijen, L. Hashemi, M. Boon, R. Farajzadeh, H. Hajibeygi, Microfluidics-based analysis of dynamic contact angles relevant for underground hydrogen storage, *Adv. Water Resour.* 164 (2022) 104221.
- [49] A.E. Yekta, J.C. Manceau, S. Gaboreau, M. Pichavant, P. Audigane, Determination of Hydrogen - Water Relative Permeability and Capillary Pressure in Sandstone: Application to Underground Hydrogen Injection in Sedimentary Formations, *Transp. Porous Media* 122 (2018) 333–356.
- [50] V. Cnudde, M.N. Boone, High-resolution X-ray computed tomography in geosciences: A review of the current technology and applications, *Earth Sci. Rev.* 123 (2013) 1–17.
- [51] M.J. Blunt et al., Pore-scale imaging and modelling, *Adv. Water Resour.* 51 (2013) 197–216.
- [52] C.A. Reynolds, H. Menke, M. Andrew, M.J. Blunt, S. Krevor, Dynamic fluid connectivity during steady-state multiphase flow in a sandstone, *Proc. Nat. Acad. Sci. USA* 114 (2017) 8187–8192.
- [53] T. Bultreys, et al., Verifying Pore Network Models of Imbibition in Rocks Using Time-Resolved Synchrotron Imaging, *Water Resour. Res.* 56 (2020) e2019WR026587.
- [54] A. Mascini, V. Cnudde, T. Bultreys, Event-based contact angle measurements inside porous media using time-resolved micro-computed tomography, *J. Colloid Interface Sci.* 572 (2020) 354–363.
- [55] N.K. Jha et al., Pore scale investigation of hydrogen injection in sandstone via X-ray micro-tomography, *Int. J. Hydrogen Energy* 46 (2021) 34822–34829.
- [56] A.E. Peksa, K.H.A.A. Wolf, P.L.J. Zitha, Bentheimer sandstone revisited for experimental purposes, *Mar. Pet. Geol.* 67 (2015) 701–719.
- [57] Z. Zhang, S. Kruschwitz, A. Weller, M. Halisch, Enhanced pore space analysis by use of  $\mu$ -CT, MIP, NMR, and SIP, *Solid Earth* 9 (2018) 1225–1238.
- [58] C. Wim Dubelaar, T.G. Nijland, The Bentheim Sandstone: Geology, Petrophysics, Varieties and Its Use as Dimension Stone, *Eng. Geol. Soc. Territory, Springer International Publishing* 8 (2015) 557–563.
- [59] Hydrogen Analysis Resource Center. <https://h2tools.org/hyarc>.
- [60] Y.T.F. Chow, G.C. Maitland, J.P.M. Trusler, Interfacial tensions of (H<sub>2</sub>O + H<sub>2</sub>) and (H<sub>2</sub>O + CO<sub>2</sub> + H<sub>2</sub>) systems at temperatures of (298–448) K and pressures up to 45 MPa, *Fluid Phase Equilib.* 475 (2018) 37–44.
- [61] A. Buades, B. Coll, J.M. Morel, Nonlocal image and movie denoising, *Int. J. Comput. Vision* 76 (2008) 123–139.
- [62] S. Schluter, A. Sheppard, K. Brown, D. Wildenschild, Image processing of multiphase images obtained via X-ray microtomography: A review, *Water Resour. Res.* 50 (2014) 3615–3639.
- [63] A.Q. Raeini, B. Bijeljic, M.J. Blunt, Generalized network modeling: Network extraction as a coarse-scale discretization of the void space of porous media, *Phys. Rev. E* 96 (2017) 013312.
- [64] H. Dong, M.J. Blunt, Pore-network extraction from micro-computerized-tomography images, *Phys. Rev. E - Stat., Nonlinear, Soft Matter Phys.* 80 (2009) 036307.
- [65] T. Bultreys et al., Validation of model predictions of pore-scale fluid distributions during two-phase flow, *Phys. Rev. E* 97 (2018) 053104.
- [66] A. Alratrout, A.Q. Raeini, B. Bijeljic, M.J. Blunt, Automatic measurement of contact angle in pore-space images, *Adv. Water Resour.* 109 (2017) 158–169.
- [67] K. Singh, T. Bultreys, A.Q. Raeini, M. Shams, M.J. Blunt, New type of pore-snap-off and displacement correlations in imbibition, *J. Colloid Interface Sci.* 609 (2022) 384–392.
- [68] A. Alratrout, M.J. Blunt, B. Bijeljic, Spatial Correlation of Contact Angle and Curvature in Pore-Space Images, *Water Resour. Res.* 54 (2018) 6133–6152.
- [69] A. Alratrout, M.J. Blunt, B. Bijeljic, Wettability in complex porous materials, the mixed-wet state, and its relationship to surface roughness, *Proc. Nat. Acad. Sci. USA* 115 (2018) 8901–8906.
- [70] L.E. Dalton, K.A. Klise, S. Fuchs, D. Crandall, A. Goodman, Methods to measure contact angles in scCO<sub>2</sub>-brine-sandstone systems, *Adv. Water Resour.* 122 (2018) 278–290.
- [71] A. Scanziani, K. Singh, T. Bultreys, B. Bijeljic, M.J. Blunt, In situ characterization of immiscible three-phase flow at the pore scale for a water-wet carbonate rock, *Adv. Water Resour.* 121 (2018) 446–455.
- [72] S. Chabab, P. Théveneau, C. Coquelet, J. Corvisier, P. Paricaud, Measurements and predictive models of high-pressure H<sub>2</sub> solubility in brine (H<sub>2</sub>O+NaCl) for underground hydrogen storage application, *Int. J. Hydrogen Energy* 45 (2020) 32206–32220.
- [73] X. Li, M. Akbarabadi, Z.T. Karpyn, M. Piri, E. Bazilevska, Experimental investigation of carbon dioxide trapping due to capillary retention in saline aquifers, *Geofluids* 15 (2015) 563–576.
- [74] M. Andrew, B. Bijeljic, M.J. Blunt, Pore-scale imaging of trapped supercritical carbon dioxide in sandstones and carbonates, *Int. J. Greenhouse Gas Control* 22 (2014) 1–14.
- [75] J.Q. Shi, Z. Xue, S. Durucan, Supercritical CO<sub>2</sub> core flooding and imbibition in Tako sandstone - Influence of sub-core scale heterogeneity, *Int. J. Greenhouse Gas Control* 5 (2011) 75–87.
- [76] M.J. Blunt, *Multiphase Flow in Permeable Media*. Cambridge University Press, 2016.
- [77] K. Singh et al., Dynamics of snap-off and pore-filling events during two-phase fluid flow in permeable media, *Sci. Rep.* 7 (2017) 5192.
- [78] Z. Jangda, et al., Pore-Scale Visualization of Hydrogen Storage in a Sandstone at Subsurface Pressure and Temperature Conditions: Trapping, Dissolution and Wettability. *figshare, Dataset*, (2022). <https://doi.org/10.6084/m9.figshare.20260968.v1>.